Continental Shelf Baroclinic Instability. Part I: Relaxation from Upwelling or Downwelling

K. H. BRINK

Department of Physical Oceanography, Woods Hole Oceanographic Institution, Woods Hole, Massachusetts

(Manuscript received 24 February 2015, in final form 12 November 2015)

ABSTRACT

There exists a good deal of indirect evidence, from several locations around the world, that there is a substantial eddy field over continental shelves. These eddies appear to have typical swirl velocities of a few centimeters per second and have horizontal scales of perhaps 5–10 km. These eddies are weak compared to typical, wind-driven, alongshore flows but often seem to dominate middepth cross-shelf flows. The idea that motivates the present contribution is that the alongshore wind stress ultimately energizes these eddies by means of baroclinic instabilities, even in cases where obvious intense fronts do not exist. The proposed sequence is that alongshore winds over a stratified ocean cause upwelling or downwelling, and the resulting horizontal density gradients are strong enough to fuel baroclinic instabilities of the requisite energy levels. This idea is explored here by means of a sequence of idealized primitive equation numerical model studies, each driven by a modest, nearly steady, alongshore wind stress applied for about 5–10 days. Different runs vary wind forcing, stratification, bottom slope, bottom friction, and Coriolis parameter. All runs, both upwelling and downwelling, are found to be baroclinically unstable and to have scales compatible with the underlying hypothesis. The model results, combined with physically based scalings, show that eddy kinetic energy generally increases with bottom slope, stratification, wind impulse (time integral of the wind stress), and inverse Coriolis parameter. The dominant length scale of the eddies is found to increase with increasing eddy kinetic energy and to decrease with Coriolis parameter.

1. Introduction

Kundu and Allen (1976) investigated the correlation length scales for subsurface alongshore and across-shelf currents over the continental shelf off Oregon at subtidal frequencies. They found (Fig. 1) that alongshore currents v are well correlated over alongshore scales of at least 80 km (the extent of the mooring array), while across-shelf currents u are uncorrelated at alongshore scales as short as 10 km. For isotropic random incompressible flow (e.g., Batchelor 1953), alongshore correlation scales for alongshore currents would be somewhat larger than for cross-shelf currents, but the discrepancy would be nowhere near as dramatic as that found by Kundu and Allen. Comparably complete measurements from other continental shelf locations have produced similar results for length scales, for example, for Peru near 15°S (Brink et al. 1980, their appendixes), off northern California (Dever 1997), off southern California (Winant 1983), and in the Middle Atlantic Bight (S. Lentz 2015, personal communication). It thus seems fairly likely that the scale discrepancy of the two velocity components may be a common property of continental shelf currents. Further, in all of these cases, the standard deviation of subtidal alongshore currents substantially exceeds (typically by a factor of around 2–3) that of the cross-shelf currents, a factor somewhat less than would be expected based on wind-driven "long-wave" scaling (e.g., Gill and Schumann 1974).

This finding of a length-scale differential conflicts with the otherwise successful coastal-trapped wave synthesis (e.g., Chapman 1987). If only wind-driven coastal-trapped waves (having linearized physics) were present, the two velocity components would have comparable length scales, and the alongshore current would have an amplitude about an order of magnitude greater than cross-shelf currents. Likewise, the theory predicts temperature or density fluctuations below the surface mixed layer that are about an order of magnitude weaker than

Corresponding author address: K. H. Brink, Department of Physical Oceanography, Woods Hole Oceanographic Institution, 266 Woods Hole Road, Woods Hole, MA 02543.
E-mail: kbrink@whoi.edu

DOI: 10.1175/JPO-D-15-0047.1

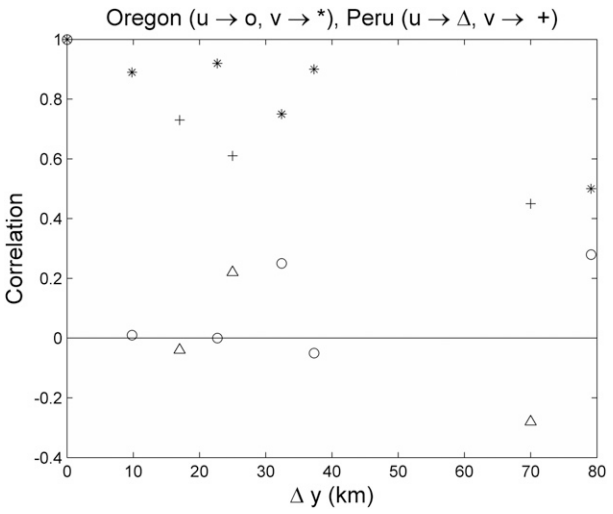

FIG. 1. Correlation of low-pass filtered cross-shelf (u: o and Δ symbols) and alongshore (v: + and *) currents as a function of alongshore separation Δy. Values are shown from both Oregon (after Kundu and Allen 1976; o and * symbols) and from off Peru near 15°S (Brink et al. 1980; Δ and + symbols).

those observed. These linear theories are successful, however, in hindcasting pressure and alongshore current variability. Thus, the forced coastal-trapped wave model, which assumes reasonably smooth topography and large spatial scales for the wind, is successful for pressure and alongshore velocity but not for cross-shelf velocity or density.

It is straightforward to express a kinematic model that is consistent with all of these findings (e.g., Brink 1987). Specifically, one can presume that alongshore currents and sea level are dominated by large-scale, wind-driven flow, as expressed by the coastal-trapped wave models and assumptions. This same wind driving would only create weak subsurface cross-shelf currents or temperature fluctuations, that is, with $\mathrm{SD}(u) = O[0.1\ \mathrm{SD}(v)]$ (where SD denotes the standard deviation at subtidal frequencies). Suppose, besides, that there is a small-scale, $O(5)$ km, isotropic eddy field with moderate $O[0.3\ \mathrm{SD}(v)]$ amplitude superimposed on this flow. Given these scales and assuming geostrophy, the pressure or sea surface height variations would be small compared to those due to large-scale wind forcing. The spatial scales of the combined flow field would be dominated by the large-scale flow for pressure or alongshore currents (since the eddy field is not large compared to the large-scale alongshore velocity), but the cross-shelf currents would be dominated by the eddy field and consequently have short, eddylike spatial scales.

While this kinematic model appears to be consistent with observations, it nonetheless tells us nothing about the origin of the eddy field. One possibility is that it is related to forcing by wind stress variations on the scale of the shelf width or smaller. While there is some evidence that wind variability on these spatial scales can affect the evolution of a preexisting ocean eddy field (e.g., Jin et al. 2009), there is also evidence that winds cannot drive flow structures that account for the observed scales (Brink et al. 1994). Another possibility is that the eddy field is associated with flow over irregular topography, although the smaller-scale eddy field is evidently found over locations with both relatively rough (e.g., northern California; Dever 1997) and smooth (Middle Atlantic Bight; S. Lentz 2015, personal communication) topography. Further, Durski and Allen (2005) show, for conditions representative of the Oregon shelf, that irregular topography complicates the eddy field associated with a shelf baroclinic instability, but it does not supersede it. Nonetheless, this possibility will be considered in a future publication. A remaining possibility is that these eddy features can be associated with baroclinic instability over the shelf. This appears to be the case during the wintertime, as shown, for example, by Pringle (2001) or Spall (2013). Pringle used a numerical model of an alongshore uniform continental shelf subject to spatially uniform wintertime cooling. Because a shallower water column cools faster than a deeper water column, a cross-shelf temperature–density gradient is rapidly established, and this, in turn, becomes baroclinically unstable on a spatial scale of $O(10)$ km. Models of this class include surface cooling but not wind forcing, and so some caution is yet required before accepting wintertime cooling as the eddy generation mechanism, although this avenue appears very promising.

The premise of the present study is that baroclinic instability is also the effective eddy-generating mechanism over the shelf even under stratified conditions. Essentially, any alongshore wind stress will generate a cross-shelf Ekman transport near the surface (in the upper roughly 20 m) and a partially compensating flow beneath. This flow pattern passes through the inner part of the shelf (exactly where depends on the spatial structure of the wind stress) so that isopycnals are warped upward or downward, depending on the wind stress direction. In either case, the sloping isopycnals are associated with a pool of gravitational available potential energy (APE) that was generated by the wind stress. Baroclinic instability can then release this available energy into an eddy field that has a scale of the baroclinic radius of deformation, that is, of $O(5–10)$ km over stratified midlatitude shelves. One aspect, involving wind-driven upwelling fronts, of this conjecture is already well studied and well accepted (e.g., Barth 1989a,b; Barth 1994; Durski and Allen 2005; Durski et al. 2007). These fronts tend to be unmistakably intense and dramatic, and so

their instability is a natural subject of inquiry. Further, there is a considerable literature on how wind forcing is associated with upwelling and baroclinic instability in the Southern Ocean [e.g., Karsten et al. (2002), to name one paper out of many], although on this larger scale, shelf topography or bottom friction would appear to be less important than in the present, coastal context. Instability in the downwelling case has not received anywhere near as much attention in the literature to date, although Feliks and Ghil (1993) do treat a quasigeostrophic downwelling structure in a configuration appropriate for the ocean offshore of the shelf. Further, linear stability results do exist for downward-sloping isopycnals near a shelf edge (Lozier et al. 2002). If wind-driven baroclinic instability is to be taken as a generally effective mechanism for small-scale shelf eddies, it needs to be shown that it can develop at appropriate amplitudes in shelf regions where downwelling can dominate, where wind-driven fronts are not obviously common, and/or where fluctuating winds (e.g., Durski and Allen 2005) give rise to an unsteady background state. One important contribution in this regard is that of Kim et al. (2009). They use simulation models to investigate explicitly the extent to which flow instabilities, evidently of the sort proposed here, contribute to observed "noise" in cross-shelf flow measurements over the Oregon shelf. Although they concluded that instabilities were not a very important factor, their grid resolution and model configuration make their results in this regard inconclusive.

The present contribution is a first step toward a further understanding of wind-driven baroclinic instability over the continental shelf. Specifically, a finite duration, unidirectional wind stress is applied to a stratified, primitive equation ocean model, and the results are tracked in order to identify and parameterize the expected current magnitude, eddy scale, and growth rates. In doing so, both upwelling and downwelling cases are treated. Once these scales are established, the next step will be a systematic study of wind-driven baroclinic instability associated with an unsteady wind forcing: a topic treated in a companion contribution (Brink and Seo 2016). In carrying out the present runs, the alongshore wind stress is kept relatively weak ($\leq 0.04\,\mathrm{N\,m^{-2}}$) in order to concentrate on fairly undramatic conditions and avoid states with extremely pronounced fronts. The modeling approach is to try to isolate the minimal physics that can account for the observed correlation scales. With this in mind, potentially complicating effects, such as irregular bottom topography, are not included in these initial contributions. Finally, a future third contribution will deal with more realistic conditions, such as observed, broadband winds, more appropriate shelf topography, bottom irregularities, and comparison with observations.

2. Methodology

a. Model configuration

All model runs employ the Regional Ocean Modeling System (ROMS; e.g., Haidvogel et al. 2000), a hydrostatic, primitive equation numerical model that uses a terrain-following vertical coordinate.

The equations of motion for the system are

$$u_t + uu_x + vu_y + wu_z - fv = -\rho_0^{-1}p_x + (Du_z)_z, \quad (1a)$$

$$v_t + uv_x + vv_y + wv_z + fu = -\rho_0^{-1}p_y + (Dv_z)_z, \quad (1b)$$

$$0 = -p_z - g\rho, \quad (1c)$$

$$u_x + v_y + w_z = 0, \quad (1d)$$

$$\rho_t + u\rho_x + v\rho_y + w\rho_z = (B\rho_z)_z, \quad \text{and} \quad (1e)$$

$$\rho = \rho_0[1 - \beta(T - T_0)], \quad (1f)$$

where u, v, and w are the cross-shelf, along-shelf, and vertical velocity components, and (x, y, z) are the corresponding coordinates. The pressure is p, T is temperature, t is time, f is the Coriolis parameter, ρ is the space- and time-dependent portion of density, ρ_0 is a constant reference density, and g is the acceleration due to gravity. Subscripts with regard to independent variables represent partial differentiation. The term T_0 is a reference temperature (14°C), the thermal expansion coefficient for water is β ($1.7 \times 10^{-4}\,^{\circ}\mathrm{C}^{-1}$), and the vertical turbulent viscosity and mixing coefficients D and B, respectively, are found using the Mellor–Yamada level 2.5 turbulence closure scheme (e.g., Wijesekera et al. 2003). The background vertical mixing and viscosity coefficients are 10^{-6} and $10^{-5}\,\mathrm{m^2\,s^{-1}}$, respectively. There is no explicit lateral mixing or viscosity in any model run.

The model is forced with a spatially uniform alongshore wind stress τ^y that ramps up over a time $t_R = 1$ day to a value of τ_A, remains steady, and then, beginning at time Δt, ramps down:

$$\tau^y = 0.5[1 - \cos(\pi t/t_R)]\tau_A \quad \text{for} \quad t < t_R, \quad (2a)$$

$$\tau^y = \tau_A \quad \text{for} \quad t_R < t < \Delta t, \quad \text{and} \quad (2b)$$

$$\tau^y = 0.5\{1 + \cos[\pi(t - \Delta t)/t_R]\}\tau_A \quad \text{for} \quad \Delta t < t < (\Delta t + t_R). \quad (2c)$$

With this time dependence, the time integral of the alongshore wind stress is then simply $\tau_A \Delta t$. The term Δt is always either 5 or 10 days (Table 1).

The bottom stress depends linearly on the bottom velocity:

$$D(u_z, v_z) = r(u, v), \quad (3)$$

TABLE 1. Model run parameters and results.

Run	$f \times 10^4\,\mathrm{s}^{-1}$	$N_0^2 \times 10^4\,\mathrm{s}^{-2}$	$r \times 10^4\,\mathrm{m\,s}^{-1}$	$\alpha \times 10^3$	Δt days	$\tau_A\,\mathrm{N\,m}^{-2}$	$\mathrm{EKE}_M \times 10^4\,\mathrm{m}^2\,\mathrm{s}^{-2}$	λ_M km	$\kappa\,\mathrm{m}^2\,\mathrm{s}^{-1}$	$\sigma_{\mathrm{NL}}\,\mathrm{day}^{-1}$
1	1.0	1.0	5.0	2.33	5.0	−0.02	1.21	13.0	1.5	0.081
2	1.0	0.5	5.0	2.33	5.0	0.02	0.71	10.6	4.5	0.055
3	1.0	1.0	5.0	2.33	5.0	0.01	0.35	11.3	7.9	0.066
4	1.0	1.0	5.0	2.33	5.0	0.02	1.67	19.7	8.3	0.115
5	1.0	1.0	5.0	3.88	5.0	0.02	1.73	15.7	10.9	0.099
6	1.0	0.5	2.0	3.88	5.0	0.01	0.14	10.3	2.7	0.106
7	1.0	1.0	5.0	1.22	5.0	0.02	0.68	12.8	13.0	0.153
8	1.0	1.0	5.0	1.22	5.0	−0.02	0.29	8.2	1.3	0.106
9	1.0	1.0	1.0	2.33	5.0	−0.02	1.18	11.5	1.4	0.066
10	1.0	0.5	5.0	2.33	5.0	−0.02	0.48	10.0	0.6	0.058
11	1.0	1.0	5.0	2.33	5.0	−0.01	0.35	10.8	1.9	0.049
12	1.0	0.5	10.0	1.22	5.0	0.04	1.28	8.6	17.6	0.197
13	1.0	0.5	1.0	1.22	5.0	0.01	0.06	5.5	3.0	0.125
14	1.0	1.0	5.0	3.88	5.0	−0.02	1.80	17.5	2.7	0.069
15	0.5	1.0	1.0	3.88	5.0	0.01	0.56	18.1	5.3	0.021
16	1.0	0.5	10.0	1.22	5.0	−0.04	0.23	6.2	1.4	0.125
17	1.0	1.0	5.0	2.33	10.0	0.02	6.60	19.5	24.6	0.153
18	1.0	0.5	2.0	3.88	5.0	−0.01	0.32	13.8	0.2	0.035
19	1.0	0.5	1.0	1.22	5.0	−0.01	0.02	3.1	0.4	0.197
20	1.0	1.0	5.0	2.33	10.0	−0.02	2.75	15.1	9.8	0.230
21	0.5	1.0	5.0	2.33	5.0	0.02	1.72	33.4	10.0	0.081
22	0.5	1.0	5.0	2.33	5.0	−0.02	3.39	34.7	17.5	0.045
23	1.0	1.0	10.0	3.88	5.0	−0.04	5.70	15.2	6.3	0.086
24	0.5	1.0	1.0	3.88	5.0	−0.01	0.60	22.6	1.3	0.115
25	0.5	1.0	5.0	3.88	5.0	−0.02	2.99	34.8	6.9	0.037
26	0.5	0.67	5.0	3.88	5.0	0.02	0.63	27.5	2.0	0.066
27	0.5	0.67	5.0	3.88	5.0	−0.02	2.27	30.0	4.3	0.034
28	1.0	1.0	10.0	3.88	5.0	0.04	6.30	22.4	1.9	0.230
29	1.0	1.0	0.2	2.33	5.0	0.02	1.13	14.9	2.2	0.069
30	0.25	0.83	5.0	2.33	5.0	0.02	0.48	43.1	0.5	0.115
31	0.25	0.83	5.0	3.88	5.0	−0.02	4.10	55.4	11.0	0.018
32	0.5	1.0	5.0	2.33	5.0	0.02	0.62	37.9	0.9	0.099

where r is a resistance coefficient. At $x = 0$, a closed, free-slip boundary condition is applied, and at the offshore boundary, there is no normal gradient for velocity, while free-surface height and temperature obey a radiation condition. All runs are initialized from a resting state, but with a small-amplitude (10^{-4} m), random free-surface height perturbation to help initiate instabilities. The initial vertical density gradient is constant at ρ_{Iz}, with buoyancy frequency N_I. There is no surface heat flux.

The model topography (Fig. 2) is simply

$$h = H_0 + \alpha x \quad \text{for} \quad x < x_1, \quad \text{and} \tag{4a}$$

$$h = H_0 + \alpha x_1 \quad \text{for} \quad x > x_1, \tag{4b}$$

where $h(x)$ is the water depth, and the field is smoothed slightly in order to remove abrupt changes in slope. The topographic width x_1 and the coastal depth H_0 are set to 45 km and 5 m, respectively, for all runs presented here.

The model uses a grid that is stretched in the cross-shelf direction so that the cross-shelf resolution is 0.15 km near $x = 0$, and it approaches 0.25 km at the offshore edge of the grid. The domain is always 54.7 km wide. The alongshore resolution is 0.15 km in all cases. All runs use 240 points in the cross-shelf direction and at least 300 points in the alongshore. In the vertical, 30 grid points are used, with a stretching that maximizes

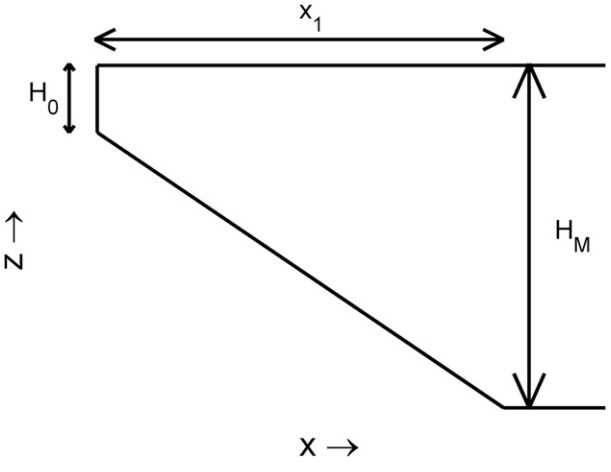

FIG. 2. Schematic of the cross-channel geometry.

resolution in the surface and bottom boundary layers. The model is cyclic in the alongshore direction, and the grid covers at least 45 km alongshore. Runs that reveal alongshore scales greater than about 20 km are repeated in a domain that is 90 km long but has the same grid resolution.

All model runs are carried out for at least 100 days. If a clear maximum in eddy kinetic energy (EKE) is not found within 100 days, the runs are extended to 200 days, by which time a clear maximum is always found.

b. Diagnostic quantities

All model statistics are computed based on an along-channel average $\{q\}$ and the deviation from this average $q'(x, y, z, t)$. Thus, the eddy kinetic energy per unit mass is

$$\mathrm{eke}(x,z,t) = \frac{1}{2}\{u'^2 + v'^2\}. \tag{5a}$$

The spatially averaged (over depth and cross-shelf distance) mean kinetic energy (MKE), eddy kinetic energy, and gravitational potential energy, all per unit mass are

$$\mathrm{MKE}(t) = \frac{1}{2A}\int_0^W\int_{-h}^0 (\{u\}^2 + \{v\}^2)\,dz\,dx, \tag{5b}$$

$$\mathrm{EKE}(t) = \frac{1}{2A}\int_0^W\int_{-h}^0 \{u'^2 + v'^2\}\,dz\,dx = \frac{1}{A}\int_0^W\int_{-h}^0 \mathrm{eke}\,dz\,dx, \tag{5c}$$

$$\mathrm{PE}(t) = \frac{1}{\rho_0 A}\int_0^W\int_{-h}^{\zeta} g\rho z\,dz\,dx, \tag{5d}$$

where $W = 40$ km, ζ is the free-surface height, and A is the (x, z) area covered by the integral. Note that the form (5d) does not lend itself to defining an eddy potential energy because $\{z\rho'\} = z\{\rho'\} = 0$. Kinetic energy dissipation (either mean or eddy) consists of two terms of comparable magnitude: an integral along the bottom boundary associated with bottom stress and a volume integral that accounts for dissipation within the water column (primarily in the bottom boundary layer). Because the system is dissipative and has an open offshore boundary, it is important to note that integrated energy is never conserved.

For each time step, the available potential energy recorded is calculated by first computing the total potential energy [(5d)] for $x = 0$ to W. Then, the density field and free surface are rearranged using a point-by-point sorting algorithm so that the surface and isotherms are flat and the water column is stably stratified. At this point, the total potential energy [(5d)] is again calculated. The difference of the two numbers is the APE. This approach is similar to that of Winters et al. (1995).

Two useful diagnostic quantities are the spatially averaged conversion (per unit mass) of potential to kinetic energy,

$$C_{\mathrm{PE}\to\mathrm{KE}} = -\frac{g}{\rho_0 A}\int_0^W\int_{-h}^0 \{w\rho\}\,dz\,dx = -\frac{g}{\rho_0 A}\int_0^W\int_{-h}^0 (\{w\}\{\rho\} + \{w'\rho'\})\,dz\,dx, \tag{6a}$$

and the conversion from mean kinetic energy to eddy kinetic energy,

$$C_{\mathrm{MKE}\to\mathrm{EKE}} = -\frac{1}{A}\int_0^W\int_{-h}^0 (\{v_x\}\{u'v'\} + \{v_z\}\{w'v'\} + \{u_x\}\{u'u'\} + \{u_z\}\{w'u'\})\,dz\,dx. \tag{6b}$$

The $\{w\}\{\rho\}$ term in (6a) is expected to dominate during wind-driven up/downwelling or during geostrophic adjustment, while the eddy term $\{w'\rho'\}$ is important during baroclinic instability. The kinetic energy conversion (6b) is typically dominated by the two terms that involve mean along-channel flow $\{v\}$, and the terms involving horizontal Reynolds stresses are indicative of barotropic instability, while terms involving vertical Reynolds stresses are indicative of Kelvin–Helmholtz instability. In addition, other terms, associated with cross-shelf fluxes at $x = W$, affect the evolution of EKE within the control volume, but these are generally small and thus not discussed here.

In addition, the dominant along-channel wavelength $\lambda(x, t)$ is estimated using the along-channel covariance of the cross-channel velocity, averaged over near-surface and middepth currents within 1 km of a nominal x location. The actual wavelength is defined as 4 times the distance to the first zero crossing of the averaged autocovariance function. This definition is particularly useful during the earlier stages of an instability when the along-channel fluctuations tend to be monochromatic. In addition, the degree of depth dependence in the eddy field is characterized by a ratio of rms velocity difference relative to rms velocity in the upper half of the water column Γ (defined, e.g., by Brink and Cherian 2013). This ratio is >1 for strongly baroclinic flow and approaches 0 as flow becomes depth independent.

c. Nondimensional numbers

Defining some nondimensional numbers helps to clarify the parameter space that needs to be considered and aids in generalizing the model results. A starting point is to develop a scale v^* for a typical alongshore velocity. Neglecting alongshore variations, assuming a

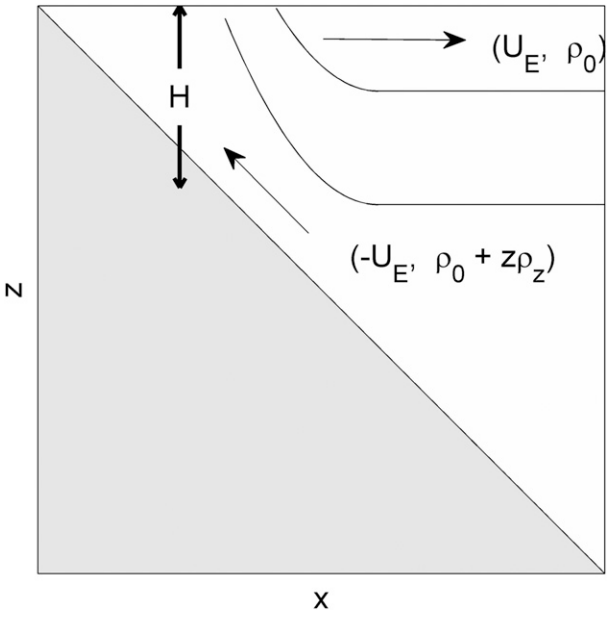

FIG. 3. Schematic of an initial, two-dimensional, upwelling configuration.

relatively long frictional time scale, using the applied wind stress, and taking a time integral of the first and last terms in (1b), a reasonable estimate for this velocity scale is

$$v^* = |\tau_A|\Delta t(\rho_0 H)^{-1}, \tag{7}$$

where H is a representative depth scale. Following Austin and Lentz (2002), the depth scale is taken to be the outer depth of the nearshore region where the initial waters are replaced by waters from offshore (Fig. 3). (Although this figure is drawn for an upwelling context, an analogous cartoon for a downwelling case would lead to the same scale estimates.) Specifically, the offshore flux of water in either the surface boundary layer or below it is the Ekman transport $U^* = O[|\tau_A|(\rho_0 f)^{-1}]$, and the cross-sectional area of water brought into the nearshore region is then the time integral of U^*. This area is then [from (4) and neglecting H_0] roughly $0.5H^2/\alpha$. Equating these areas (and dropping the factor of 0.5 because this is just a scaling) yields

$$H = [\alpha|\tau_A|\Delta t(\rho_0 f)^{-1}]^{1/2}. \tag{8}$$

This can be thought of as the isobath at which (roughly) an incipient upwelling or downwelling front would be located. Combining (7) and (8) gives an estimate for a typical alongshore velocity at the front before the onset of instability:

$$v^* = [f|\tau_A|\Delta t(\rho_0 \alpha)^{-1}]^{1/2}. \tag{9}$$

Frictional effects are measured via

$$\Omega = r(fH)^{-1} = r\rho_0^{1/2}(\alpha f|\tau_A|\Delta t)^{-1/2}, \tag{10}$$

a measure that is comparable to the square root of an Ekman number. The frictional parameter required for parameterizing buoyancy arrest is

$$d = c_D N_I f^{-1} \approx r N_I (fv^*)^{-1}, \tag{11}$$

where c_D is a drag coefficient appropriate for use in a quadratic estimate of bottom stress. Finally, the slope Burger number is

$$s = \alpha N_I f^{-1}. \tag{12}$$

The last two definitions will be useful to readers relating present results to those of Brink and Lentz (2010).

3. Results

a. *Specific examples*

It is useful first to consider the evolution of two representative model runs: 1 (downwelling) and 4 (upwelling). The two runs are identical except for the sign of the wind stress (Table 1). This pair of runs is typical of all others in that flow initially (for 0–20 days) behaves essentially two-dimensionally and then becomes unstable, reaching a well-defined peak in EKE at some point during the model run. The parameter values for these two runs (s = 0.23) are intermediate between summertime conditions in the Middle Atlantic Bight and off northern California. Other runs in Table 1 were chosen to explore the effects of rotation, stratification, stress amplitude, bottom slope, and bottom friction.

Typically, the system behaves largely two-dimensionally during the time that wind forcing is applied, so that, by the end of the forcing period (day 6 here), fairly classical patterns emerge (Fig. 4). In the downwelling case (run 1), there is a broad maximum in alongshore flow, and the temperature does not show any pronounced frontal structures. The bottom boundary layer is about 20 m thick, and the buoyancy arrest time scale [Brink and Lentz 2010, their (26)] is estimated to be about 12 days, that is, somewhat longer than the time of wind-forced cross-shelf transport. For the various runs in Table 1, the arrest time scale varies from less than a day to more than 1000 days. In all cases, however, the depth-integrated cross-shelf volume flux has to be approximately zero. What does change is whether the subsurface flow that compensates surface Ekman transport occurs within or above the bottom boundary layer.

Although no front is obvious for downwelling, substantial lateral density gradients, representing a pool of

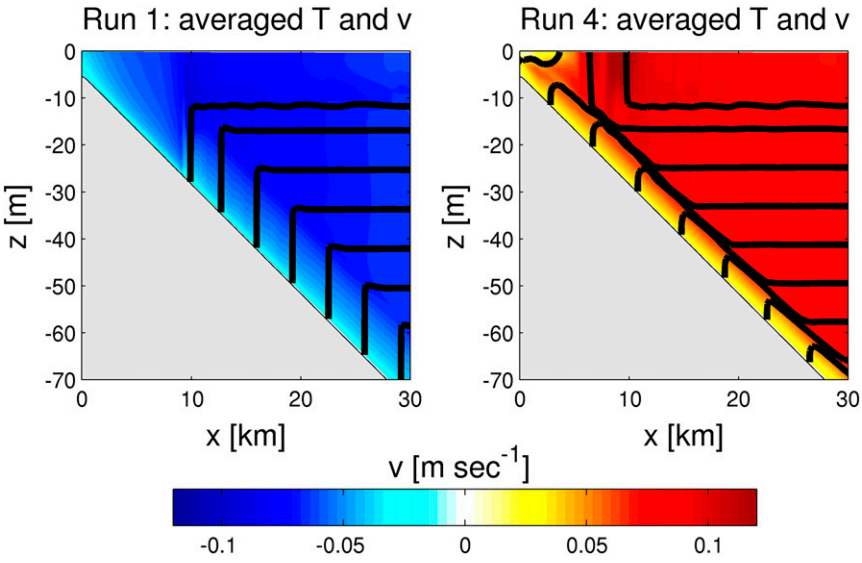

FIG. 4. Cross-channel sections of temperature (heavy contours: interval = 0.5°C) and along-channel velocity (color) at $t = 6$ days. The wind forcing has just stopped and instabilities are not yet detectable. Only the innermost 30 km of the shelf are shown. (left) Run 1, with downwelling-favorable winds and negative alongshore flow. (right) Run 4, with upwelling-favorable winds and positive alongshore flow but otherwise exactly like run 1.

available potential energy, do develop nearshore and in the lower part of the water column. In the upwelling case (run 4), an identifiable front and related alongshore jet do form in the upper part of the water column: a structure that is likely to be unstable, based on previous results (e.g., Barth 1989a; Durski and Allen 2005). The bottom boundary layer is relatively thin (about 5 m) and has a sharp cap. The buoyancy arrest time scale for this case [Brink and Lentz 2010, their (44)–(45)] is about 4–5 days, so that the bottom stress should be partially neutralized.

Energetically, the MKE grows initially for both runs (Fig. 5) primarily due to wind input, although dissipation (about equally interior and bottom stress) is substantial and the cross-shelf/vertical circulation drives gravitational potential energy changes. Potential energy increases in the case of downwelling and decreases in the case of upwelling. In either case, the advective potential energy change dominates that due to turbulent vertical mixing. In both cases, APE, essentially a gross measure of lateral density differences, reaches its peak around day 10–15 (Fig. 5). The lag between wind cessation and peak APE is mainly attributable to the lateral PE flux continuing for a few days after the wind ceases. In the strictly two-dimensional limit, buoyancy arrest occurs, and so mean kinetic energy remains essentially unchanged after around day 20 (Fig. 6), while interior mixing leads to an extremely slow increase in potential energy and decrease in available potential energy.

Although runs 1 and 4 appear to be two-dimensional until around day 10, instability is already developing. Growth rates are estimated by fitting 3-day segments of the time series EKE(t) to a natural logarithm. These ''instantaneous'' growth rates are maximal at days 6.5 for run 1 and 4.5 for run 4. In both cases, the wavelength of this initial instability is 1.7 km. Although the instability is growing rapidly at this point, it is still too weak to be apparent in property maps or sections, although finite amplitude is reached by day 10 (Fig. 5).

In accord with the previous two-dimensional models of wind-driven downwelling over a slope (e.g., Allen and Newberger 1996), there is an initial stage of finite-amplitude symmetric instability in the bottom boundary layer for run 1. Typically, these two-dimensional (x and z) rolls first become visible just offshore of the region of complete vertical homogenization (i.e., around $x = 10$ km in Fig. 4), and they then spread slowly offshore. Generally, the rolls have a cross-shelf wavelength of 1–2 km, and their vertical scale is roughly defined by the bottom boundary layer thickness. This instability, however, is no longer detectable once the more energetic baroclinic instability reaches finite amplitude (around day 10 for run 1). Baroclinic instabilities are characterized by the presence of alongshore variations and by larger offshore and vertical scales. A similar overpowering of finite-amplitude symmetric instability was also found in a model of a tidal mixing front (Brink and Cherian 2013).

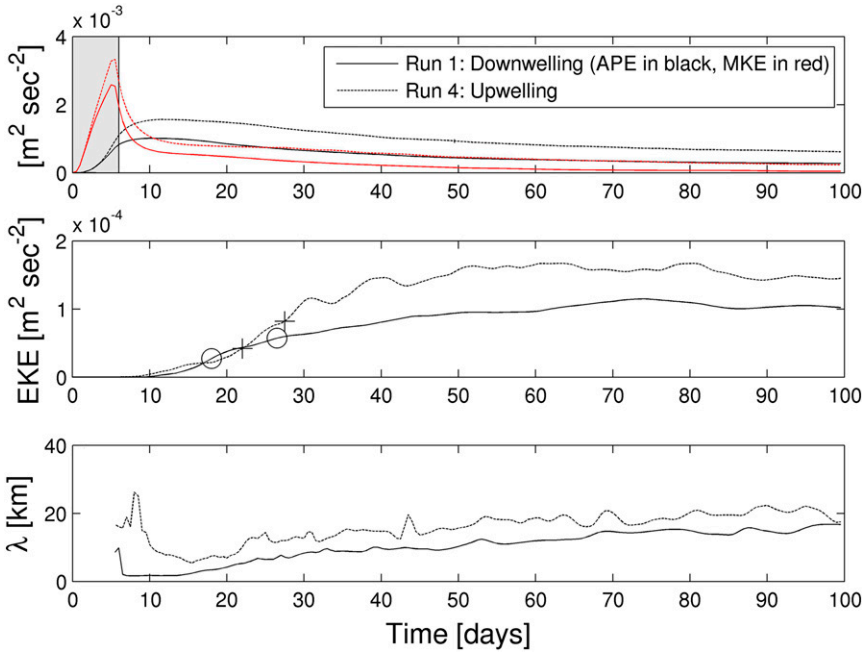

FIG. 5. (top) Spatially averaged available potential energy per unit mass (black lines) and mean kinetic energy (red lines) as a function of time for runs 1 (solid) and 4 (dashed). The shaded area represents the time over which the alongshore wind stress is applied. (middle) Averaged eddy kinetic energy [(5c)] vs time for runs 1 (solid line) and 4 (dashed line). Note the change in scale on the vertical axis. The symbols in the middle plot are at times where integrated eddy kinetic energy is one quarter (circle) and one half (+) of the peak value. (bottom) Dominant along-channel wavelength at $x = x_M$ (the offshore location of the maximum in eddy kinetic energy) vs time. The first few days of λ estimates are deleted because they are extremely noisy when the instability has very small amplitude.

The model energetics provide some insight as to what is happening (Figs. 5, 6). Throughout the following, it is found that the free-surface contribution to APE is about two or more orders of magnitude smaller than that associated with horizontal density gradients, so its contribution to APE is negligible. Regardless of the wind direction, APE increases rapidly over the first 10 days, even after the wind stress stops acting on day 6. Typically, the maximum APE, denoted as APE_M, occurs within the first 15 model days, and the maximum value is well correlated (0.98 calculated for all runs in Table 1) with the value at the end of the wind forcing period. The continued APE growth after the wind cessation is evidently associated with geostrophic adjustment and with the cross-shelf transport not halting immediately. In contrast, MKE reaches a peak around the time of wind cessation and then begins a slow frictional decay. Finally, it is worth noting that the maximum APE is somewhat greater for the upwelling run (run 4) than it is for the downwelling run (run 1), even though the runs are identical except for wind direction (averaged over all paired model runs, the upwelling APE is about 40% greater than the downwelling APE). Given the structural difference between the early stage temperature fields in the two cases (Fig. 4), it is not surprising that the exact energy levels should differ.

The eddy kinetic energy typically grows for some tens of days, and this growth is accompanied by an increase in the dominant wavelength (Fig. 5). The energy source in these runs is clearly baroclinic instability, as is apparent because the potential to kinetic energy transfer [(6a)] clearly exceeds the mean to eddy kinetic energy transfer [(6b)] during the growth phase (Fig. 7). Typically during these runs, the pool of potential energy [(5d)] decreases, but there is not a balance of this decrease against total kinetic energy increase, primarily because of dissipative effects at and near the bottom. Buoyancy arrest appears to be ineffective for the eddies, a result consistent with the arrest length scales established by Brink (2012). EKE changes due to processes within the control volume, while exchanges across the open boundary have little effect on its evolution. EKE eventually peaks at $t_M = 74$ and 80.5 days for runs 1 and 4, respectively, and the maximum values EKE_M are within about 30% of each other. It is rather striking that the two different initial configurations (Fig. 4) ultimately release comparable levels

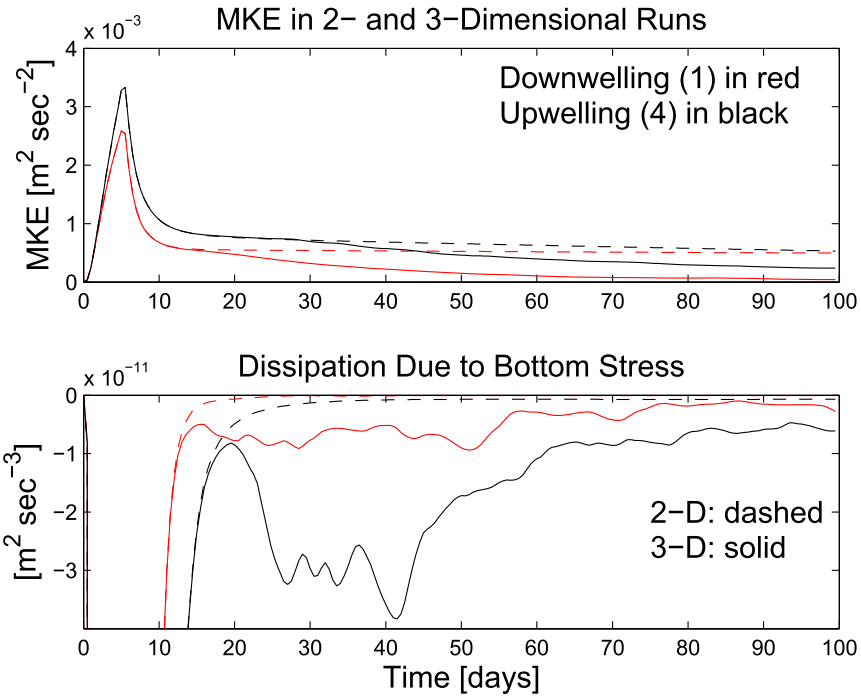

FIG. 6. (top) Time series of MKE per unit mass and (bottom) MKE dissipation rate due to bottom stress in two-dimensional (dashed) and three-dimensional (solid lines) runs. The red curves correspond to run 1 and its two-dimensional twin, while the black lines are for run 4 and its twin.

of eddy energy. After EKE reaches its peak, it slowly declines while the eddy scale continues to increase gradually.

Interestingly, in three-dimensional runs, the along-channel-averaged flow does not undergo buoyancy arrest so that the along-channel average of bottom stress does not vanish and $\{v\}$ above the bottom boundary layer thus dies away with time after around day 20 (Fig. 6). The contrast with the two-dimensional case is particularly clear when comparing time series of MKE and MKE dissipation due to bottom stress (Fig. 6). This failure to arrest seems consistent with the underlying nonlinearity: the short scales associated with the eddy field prevent arrest on the eddy length scale (e.g., Brink 2012), and they also appear to prevent arrest on the larger scale that might otherwise experience arrest in the absence of eddies. Why this should be so is not obvious, but a similar result was also found in another multiscale context (Brink 2011).

It is important to note that even the maximum EKE is only a fraction (typically, across all runs, about 15%) of the maximum APE or MKE. For example, for run 1 (4), the maxima of EKE, APE, and MKE are 0.12×10^{-3}(0.17×10^{-3}), 1.0×10^{-3} (1.6×10^{-3}), and 2.6×10^{-3}(3.3×10^{-3}) $\mathrm{m^2\,s^{-2}}$, respectively (Fig. 5). Why should that be? Part of the answer is that some of the APE remains in place: it is not all used up. However, kinetic energy dissipation (Fig. 7) assures that the system is not conservative.

It is useful to have an estimate for the gross EKE growth rate during finite-amplitude evolution. At this stage, the 3-day exponential fits yield noisy estimates and values substantially lower than during the initial phases. Another possible measure of growth rate would be the time t_M at which maximum EKE is reached. The flatness of this maximum (Fig. 5, middle panel), however, makes this estimate quite noisy also. A somewhat better solution is to record the times, $t_{1/4}$ and $t_{1/2}$, at which EKE is a quarter and a half, respectively, of its maximum value EKE_M. These times are marked by circle or plus symbols in Fig. 5 for runs 1 and 4, respectively. The times are chosen because they generally fall during the interval when EKE is growing roughly exponentially. It is then straightforward to estimate a representative exponential growth rate for the finite-amplitude phase:

$$\sigma_{\mathrm{NL}} = \ln(2)(t_{1/2} - t_{1/4})^{-1}, \tag{13}$$

and it is these values that are tabulated in Table 1. The irregularity in EKE growth (see Fig. 5) still makes these estimates noisy, but the estimates do appear credible. For runs both 1 and 4, the growth time $\sigma_{\mathrm{NL}}^{-1}$ is roughly 10 days. This can be compared to Barth's (1994) finite-amplitude

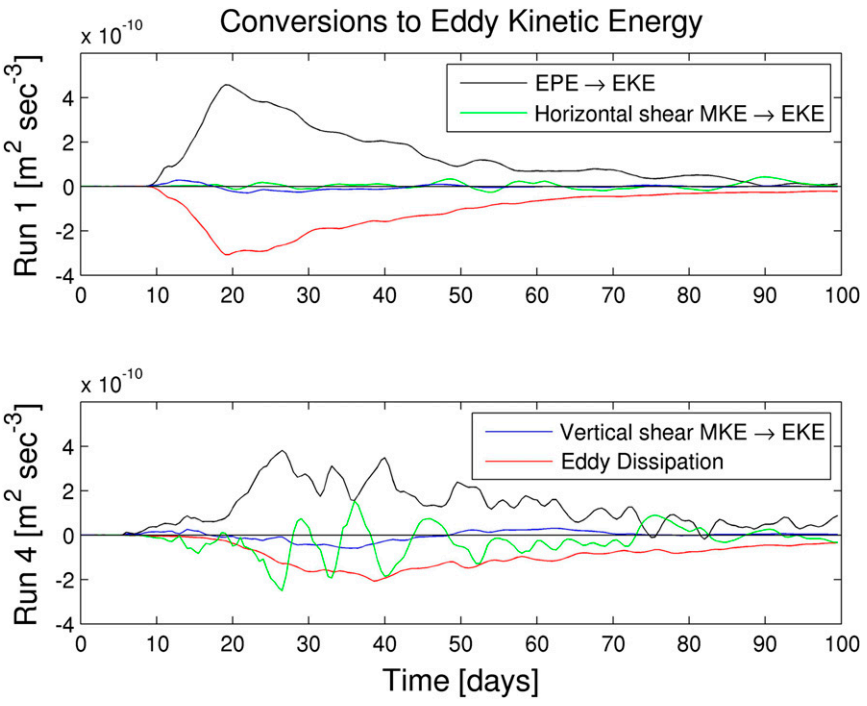

FIG. 7. Conversions to eddy kinetic energy vs time for runs (top) 1 and (bottom) 4. The lines represent eddy conversion from potential to kinetic energy [black: $\{w'\rho'\}$ term in (6a)], the green line represents mean to eddy kinetic energy conversion associated with horizontal alongshore shear in (6b), the blue line represents mean to eddy kinetic energy conversion associated with alongshore vertical shear in (6b), and the red line is the dissipation of eddy kinetic energy.

value of perhaps 3 days or Durski and Allen's (2005) time scale of perhaps 5 days. Both of these comparisons are inexact, however, because of the former's simple geometry and the latter's sustained wind forcing.

Some appreciation of the spatial structures can be gained by considering flow properties averaged alongshore and over 7 days centered on the time of maximum EKE, that is, $t = t_M$ (Figs. 8 and 9). In both cases, the maximum mean alongshore velocity is a good deal weaker than at the time of wind cessation (Fig. 4), and the alongshore flow is fairly broadly distributed. The mean isotherms in both cases slope in the same sense as initially but far more gently than in the initial state. If the bottom were completely flat, one would expect that the ultimate steady state would be characterized by completely flat isotherms so the available potential energy of the initial (here meaning after the wind ceases but before instability becomes substantial) state (Fig. 4) would be exhausted. However, the Charney–Stern–Pedlosky theorem (Charney and Stern 1962; Pedlosky 1964a,b) states that a stable state has to have isotherms parallel to the boundaries at the surface and bottom when the velocity shear is nonzero. (Although this theorem applies to the quasigeostrophic limit, one might expect it to hold more generally, at least qualitatively.) Thus, sloping isopycnals are perhaps expected in any final, stable state that has a vertically sheared mean alongshore flow, and there is no reason to expect that, with a sloping bottom, the APE will vanish with time, that is, the initial available potential energy implicit in Fig. 4 need not be completely consumed.

The eddy kinetic energy spatial distributions (right panels of Figs. 8 and 9) always show strong depth dependence, but they differ dramatically between the upwelling and downwelling configurations. In the upwelling case (Fig. 9), the spatial maximum in eddy energy lies at the surface above the most strongly sloping isotherms and slightly inshore of the maximum mean alongshore velocity. In the downwelling case (Fig. 8), the extreme values of eke are not as large, but the energy is distributed more broadly in space. Specifically, the maximum energy is found in a tongue extending downward and offshore just above the bottom boundary layer. The shallow expression of the eddy field is only substantial where this tongue intercepts the surface. The rationalization for these distributions appears to be simply that current variability concentrates roughly where horizontal density gradients (hence available kinetic energy) occur at the cessation of

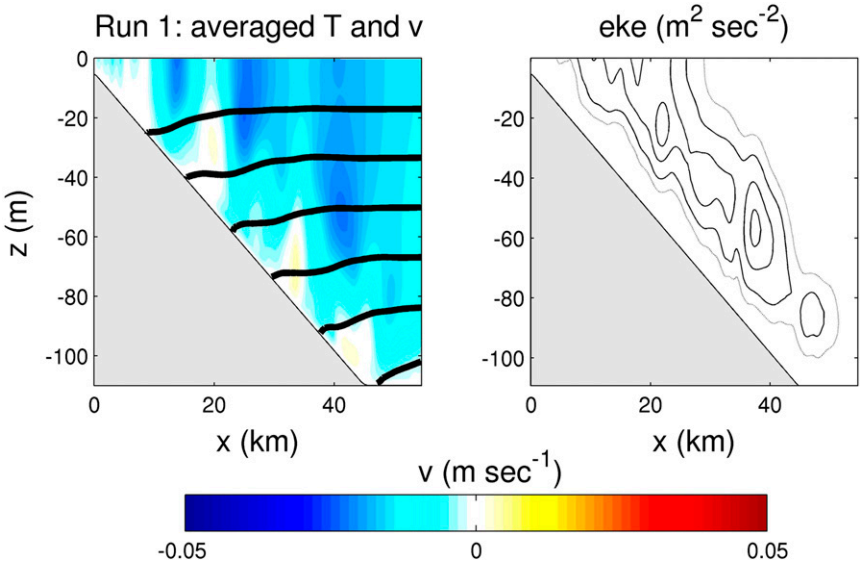

FIG. 8. Flow statistics for a 7-day average centered on the time, $t_M = 74$ days, of maximum spatially averaged eddy kinetic energy for run 1. (left) Mean temperature (heavy contours: interval = 1°C) and along-channel velocity magnitude (color). (right) eke, with the contour interval being $1 \times 10^{-4}\,\mathrm{m^2\,s^{-2}}$ for the solid black contours. In addition, $0.5 \times 10^{-4}\,\mathrm{m^2\,s^{-2}}$ is shown by a lighter contour.

the wind forcing, that is, eddy kinetic energy develops in spatial proximity to where the available potential energy resides (cf. Figs. 8 and 9 with Fig. 4).

The horizontal distribution of the eddies is exemplified by Fig. 10, which shows a snapshot of the surface temperature and velocity for run 4 at time $t = t_M$. Cooler water is found closer to shore, as would be expected as a result of upwelling, but the striking aspect of the figure is the offshore variation in the eddy scale. Nearshore, the scales are fairly small (around 5 km), but farther offshore the scales are larger and dominated by a few relatively isotropic isolated vortices with swirl velocities of $O(0.1)\,\mathrm{m\,s^{-1}}$. This visual impression is borne out by calculating the wavelength as a function of offshore distance (Fig. 11). The dominant wavelength increases monotonically until the vicinity of $x = x_M$ (the offshore location of maximum eke, which occurs at $z = z_M$). Offshore of x_M, the length scale decreases somewhat but

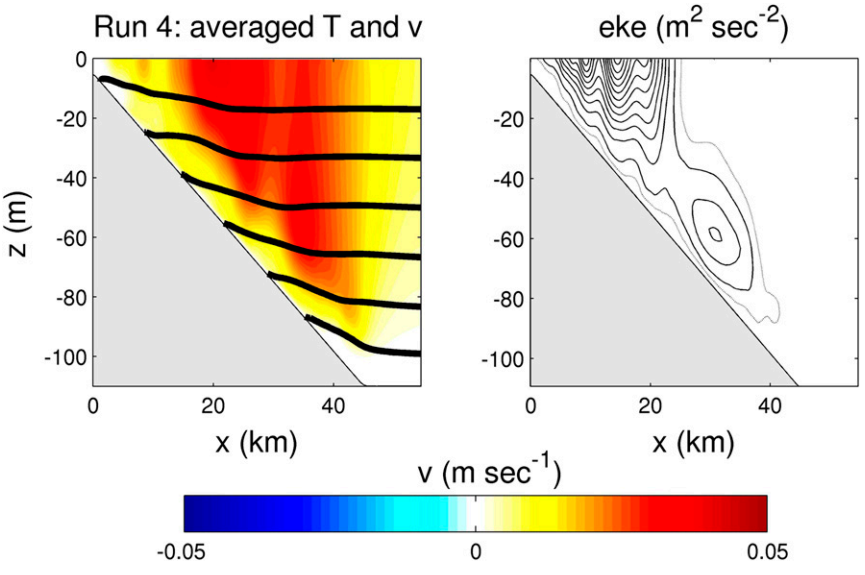

FIG. 9. As in Fig. 8, but for $t_M = 80.5$ days for run 4.

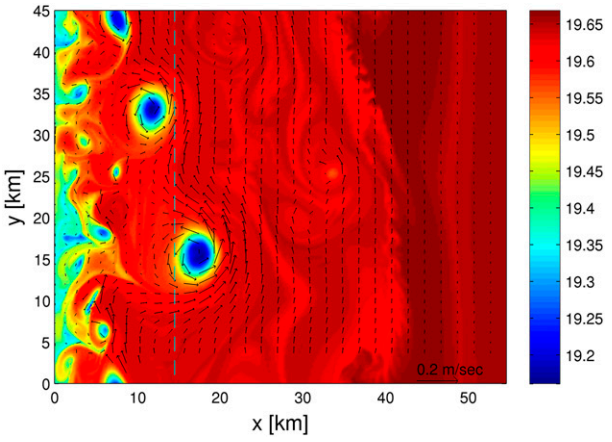

FIG. 10. Snapshot of surface temperature (color) and velocity for run 4 at $t = t_M = 80.5$ days. The location $x_M = 14.5$ km is shown as a dashed cyan line.

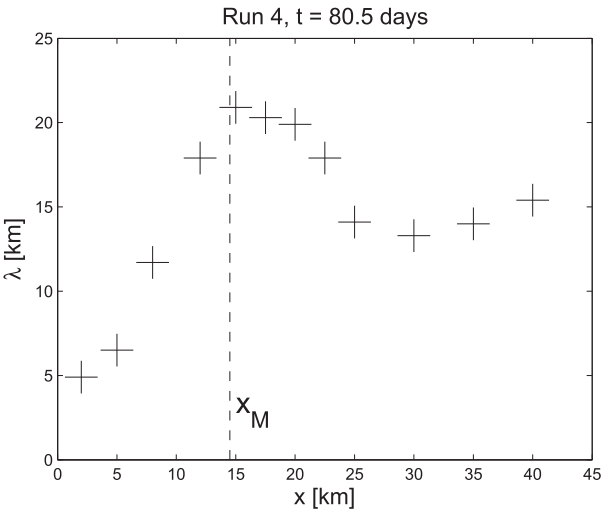

FIG. 11. Dominant along-channel wavelength λ as a function of distance offshore for run 4 at $t = t_M = 80.5$ days. The offshore distance x_M is where eke is at a maximum. This can be compared with Fig. 10.

not dramatically. Very similar results are found for run 1, the only substantial difference being that the warmest water is found nearshore rather than offshore. To be precise in the face of this spatial structure, the tabulated wavelengths λ_M (M standing for at the time of the maximum EKE) in Table 1 are consistently estimated at offshore distance x_M and time t_M for each calculation.

Typically, by the end of an upwelling model run (such as 4), the averaged (over 7 days and along channel) temperature distribution shows flat isopycnals over most of the domain, but an upwarping toward the coast within about 20 m of the bottom. No bottom mixed layer is ever apparent. For downwelling runs, the system adjusts to a mean condition of flat isotherms near the bottom boundary and far offshore, bridged by a gentle, weak downward (toward the coast) slant in between. This is not an end state that would be immediately anticipated by either buoyancy arrest or stability considerations. However, flat isotherms are consistent with an absence of APE, hence baroclinic stability. These trends for isotherm slope are already clearly developing at $t = t_M$ for runs 1 (Fig. 8) and 4 (Fig. 9).

One very simple way to assess the impact of these eddy fields is to quantify their importance for horizontal mixing. This is done by estimating the eddy diffusivity centered at time t_M and for a 5-km range of locations centered at x_M. At each depth in this x range, an 8-day average eddy diffusivity is calculated as

$$\kappa = -\{u'T'\}\{T_x\}^{-1}. \tag{14}$$

Fluxes and gradients from levels with a downgradient flux are then integrated (i.e., averaged with a weight of the appropriate vertical grid spacing) to form a spatially averaged estimate κ, which is recorded in Table 1. For the downwelling (run 1) and upwelling (run 4) runs here, values of 1.5 and 8.3 $m^2 s^{-1}$ are found, respectively. These numbers are placed in context in section 5.

b. *Qualitative trends*

Before treating scalings to summarize the model outputs, it is useful to explore qualitatively how model results differ among runs. Runs 1 and 4, discussed above, are reasonably typical in most regards, although some departures are found. For example, if the wind stress is applied for longer periods (such as 10 days, run 17), the instability can reach finite amplitude even before the wind stress stops acting. However, all model runs show the common features of instability growth, an EKE maximum, length scale increase with time, and clearly depth-dependent eddy fields (typically $\Gamma = 0.4$–1 at $t = t_M$, $x = x_M$).

Some patterns in parameter dependence are immediately apparent in Table 1. For example, the dominant wavelength λ_M increases as the initial buoyancy frequency increases: see runs 2 versus 4 for upwelling conditions and runs 10 versus 1 for downwelling. Similarly, λ_M decreases as f increases (see runs 21 vs 4 or 22 vs 1). This length scale dependence is what one would expect if the internal Rossby radius were the appropriate scale. There is some evidence that the dominant wavelength increases as the bottom slope increases (e.g., downwelling runs 8 vs 14 vs 1), but this is not consistently the case (e.g., the comparable upwelling runs 6 vs 4 vs 5).

The maximum eddy kinetic energy EKE_M increases strongly as the buoyancy frequency increases (e.g., runs 2 vs 4 or 10 vs 1). It also increases as the bottom slope

increases (runs 8, 14, and 1 or 6, 4, and 5) or as the forcing time Δt increases (runs 4 vs 17 or 1 vs 20). These trends make sense in that one expects extended wind forcing or enhanced stratification to lead to more available potential energy (larger horizontal density contrasts) at the early stages of the model runs. Interestingly, the trend is less obvious when it comes to bottom friction: increasing r increases EKE_M for an extreme upwelling comparison (runs 29 vs 4), but increasing r has no obvious effect in a downwelling comparison (runs 9 vs 1).

Other, comparable, qualitative comparisons of outputs are, of course, possible, but, in many cases they yield ambiguous results or simple comparisons are difficult because more than one parameter is changed at a time. A scaling analysis will help to clarify these dependencies.

4. Scaling

a. Eddy kinetic energy

In all model runs, the potential to kinetic energy conversion plays an important, generally dominant, role for fueling the growth of EKE. It thus makes sense to treat the scaling in terms of baroclinic instability by starting with an estimate of the available potential energy at the moment when the wind forcing ceases.

Consider a cartoon for the upwelling case (Fig. 3). As a first approximation, assume that, by the end of the wind forcing period, all of the inner shelf water has been replaced by upwelled waters (density of order $\rho_0 + H\rho_{Iz}$) from offshore. The cross-sectional area of the homogeneous nearshore water simply reflects the time-integrated onshore Ekman transport:

$$U_E \Delta t = |\tau_A| \Delta t (\rho_0 f)^{-1}. \tag{15}$$

Treating the inshore waters as a wedge (i.e., taking $H_0 \approx 0$), the water depth at the offshore edge of the homogenous patch is given by (8), and so a typical density difference between inner shelf and shelf water is $\Delta\rho = O(\rho_{Iz} H)$. In both the early and later (buoyancy arrested) stages of the flow evolution, the deeper, cross-shelf flow will occur in the interior of the water column, so that $\Delta\rho \approx 0.25\rho_{Iz} H$ might be a more exact estimate of the density contrast. On the other hand, if the compensating flow is in the bottom boundary layer, $\Delta\rho \approx 0.5\rho_{Iz} H$ might be a better estimate. In any case, the factor of 0.25 or 0.5 is not imposed [i.e., (16) simply uses $\Delta\rho \approx \rho_{Iz} H$], but an empirical constant is found subsequently. The anomaly in potential energy per unit mass (compared to an ocean with completely flat isotherms) is then the average of $zg\Delta\rho\rho_0^{-1} \approx 0.5Hg\Delta\rho\rho_0^{-1}$. One thus expects the magnitude of the spatially averaged APE per unit mass to be

$$E_0 \approx \alpha N_I^2 |\tau_A| \Delta t (2\rho_0 f)^{-1}. \tag{16}$$

A similar argument leads to the same APE scaling in the downwelling case. It may seem odd that the APE associated with bottom boundary layer density gradients is apparently not accounted for here. Although the total (spatially integrated) APE associated with the boundary layer is typically comparable to or larger than that in the inner shelf, the spatial density of APE (total integrated APE divided by cross-sectional area) on the inner shelf is higher by a factor of about $\alpha N \Delta t$, that is, by about an order of magnitude. This density difference appears to explain why (16) is a good basis for scaling, although it is corrected empirically below, apparently for bottom boundary layer effects. Finally, as a first approximation, one might expect that E_0 would be proportional to the maximum EKE unleashed by the instability EKE_M. However, this is found to be a poor approximation, especially for the upwelling cases ($\tau_A > 0$).

The initial scaling [(16)] is found to be a mediocre representation of APE_M, the maximum computed APE. Perhaps this is not surprising since there is nothing here that accounts for the structural differences in temperature fields during upwelling or downwelling (e.g., compare the two panels of Fig. 4). Using all model runs, a considerable improvement is obtained by multiplying (16) by an empirical factor of $(1 + \eta s^2)^{-1}$, where $\eta = 8$ for $\tau_A > 0$ and $\eta = 9$ for $\tau_A < 0$ (correlation of fit equals 0.93 and 0.97, respectively). This correction appears to help account for the portion of APE associated with up- or downslope bottom boundary layer transport, that is, for density changes occurring outside of the nearshore wedge of replaced waters. That such a correction is needed is consistent with (16), representing an average over only the inner shelf wedge even though APE is calculated out to $x = W$. Thus, boundary layer APE farther offshore needs to be accounted for, and following the scale arguments of Brink and Lentz (2010), the boundary layer–integrated buoyancy deficit [their (4f) or (11)], which is directly related to APE, is expected to decrease as s increases. Thus, the $(1 + \eta s^2)^{-1}$ form of the APE correction is qualitatively consistent with expectations based on boundary layer transport.

Once the APE is known, however, one still needs to know about its transfer to EKE. It is again found, not surprisingly, that this transfer depends upon the bottom slope. Specifically, the expression

$$\mathrm{EKE}_M = a^* \mathrm{APE}_M (1 + \mu s^2)^{-1} \tag{17}$$

is found to be a good approximation, with $a^* = 0.15$ and $\mu = 2$ for $\tau_A > 0$, and $a^* = 0.17$ and $\mu = -0.9$ for $\tau_A < 0$ (correlations of 0.95 and 0.91, respectively). Thus, the

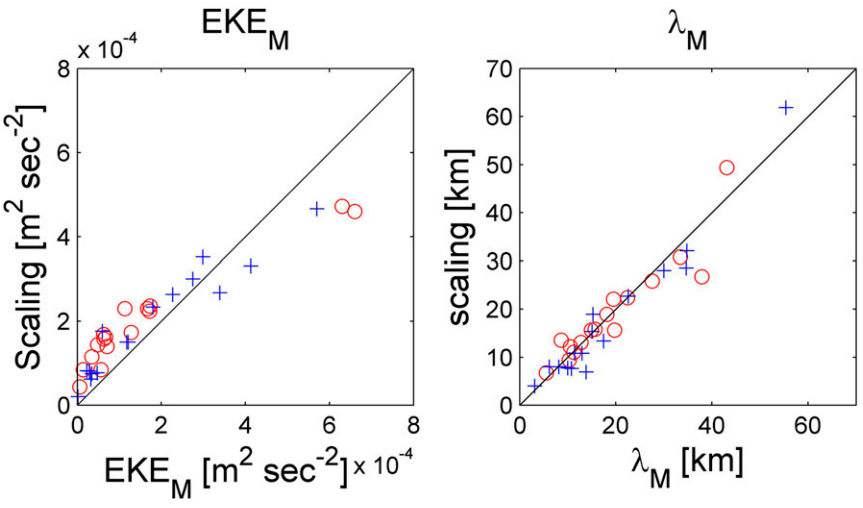

FIG. 12. Results of scaling analyses. Model results are shown on the horizontal axes, and scalings are on the vertical. Red circles show results from runs with $\tau_A > 0$, and blue crosses are for runs with $\tau_A < 0$. (left) Maximum area-averaged eddy kinetic energy EKE_M [(18)]. Correlation is 0.96 for both $\tau_A > 0$ and $\tau_A < 0$. (right) Dominant alongshore wavelength at $t = t_M$, λ_M [(19)]. Correlation = 0.93 for $\tau_A > 0$ and 0.97 for $\tau_A < 0$.

slope effect on APE is about the same for both wind directions, but, for a given APE, the slope lessens instability ($\mu > 0$) for upwelling-favorable winds, and the bottom slope destabilizes conditions ($\mu < 0$) for downwelling conditions. This behavior is contrary to the quasigeostrophic linear stability results of Blumsack and Gierasch (1972) but is consistent with the linear stability results of Barth (1989b), who accounted for finite changes in layer thicknesses. There is, of course, no strong reason for greater linear instability to require larger energy at finite amplitude.

To develop a practical scaling for EKE_M, the two slope corrections [for APE and for the APE to EKE conversion; (17)] are combined to

$$\mathrm{EKE}_M \approx a_1^+ E_0 (1 + b^+ s^2)^{-1} \quad \text{for} \quad \tau_A > 0 \qquad (18a)$$

and

$$\mathrm{EKE}_M \approx a_1^- E_0 (1 + b^- s^2)^{-1} \quad \text{for} \quad \tau_A < 0. \qquad (18b)$$

The a and b parameters are found by separate least squares fits to (18a) and (18b) using all of the runs summarized in Table 1, that is, using 16 runs for each wind stress direction. The results are encouraging for $\tau_A > 0$, $(a_1^+, b^+) = (0.036, 10)$, and the fit has a correlation of 0.96 with an rms error of $9.6 \times 10^{-5}\,\mathrm{m^2\,s^{-2}}$. For $\tau_A < 0$, $(a_1^-, b^-) = (0.016, 0.8)$ with a correlation of 0.96 and rms error of $5.9 \times 10^{-5}\,\mathrm{m^2\,s^{-2}}$ (Fig. 12, left panel). Thus, as expected, the upwelling case is much more strongly stabilized by the bottom slope than is the downwelling case, that is, $b^+ >> b^-$. However, $a_1^+ > a_1^-$, consistent with the upwelling configuration having more initial APE than the downwelling case.

There is one curious aspect to the scaling [(18)]: the absence of any dependence on the bottom friction. All of the model runs use a nonzero value of the bottom resistance coefficient, and in some cases, the value is very substantial, for example, $r = 10 \times 10^{-4}\,\mathrm{m\,s^{-1}}$ (for runs 12, 16, and others), yielding a local value of Ω as large as 2 in the shallowest water. Various attempts were made to include a frictional correction to the expressions [(18)], yet none was found that reduced the error of the fit by more than a couple percent. One possible explanation for this finding is that the fully developed eddy field at time t_M has adjusted so that velocities are near zero at the top of the bottom boundary layer, as might be expected from a stratified spindown problem (e.g., Holton 1965a,b). This mechanism appeared to apply for the instability of an idealized tidal mixing front (Brink and Cherian 2013), but it is not an adequate explanation here because the frictional dissipation remains substantial (Fig. 7).

b. Eddy length scale

Although several possible scalings based on the internal Rossby radius of deformation were attempted, the most successful scaling for the alongshore wavelength comes from hypothesizing that it scales as an inertial radius $v^* f^{-1}$, where v^* is now a representative eddy swirl velocity. Since a reasonable scale for v^* is $\mathrm{EKE}_M^{1/2}$, it then follows that

$$\lambda_M \approx a_3 \mathrm{EKE}_M^{1/2} f^{-1} \approx a_2 E_0^{1/2} f^{-1} (1 + bs^2)^{-1/2}, \quad (19)$$

where b^+ and b^- are the estimates based on (18). The scaling from (19) for the most dominant wavelength at $t = t_M$ is evaluated separately for the upwelling and the downwelling runs. The result is that for $\tau_A > 0$, $a_2^+ = 20$, and the fit has a correlation of 0.93 and an rms error of 3.8 km. For $\tau_A < 0$, $a_2^- = 11$, and the fit has a correlation of 0.97 with an rms error of 3.5 km (Fig. 12, right panel).

c. Growth rate

Knowledge of the growth rate for finite-amplitude disturbances might be expected to be important in a problem with fluctuating wind forcing. One would expect that if eddies grow slowly relative to the period of the wind forcing, there would be insufficient time for an eddy field to develop. Estimating a finite-amplitude growth time from model outputs is problematic in practice because of the irregularity in eddy development, but the estimate σ_{NL} [(13)] is apparently useful with an uncertainty of a few tens of percent.

The scaling approach is to assume that the growth rate is proportional to a representative eddy time scale. This choice makes sense for two reasons. First, one could create a scaling to estimate the initial growth rate associated with linear stability, but experience (e.g., Barth 1994) shows that, for problems like this, the initial linear instability is quickly overtaken by a finite-amplitude (meaning that the fluctuations have the same magnitude as the initial fields) eddy field that has larger scales and continues to grow and evolve. Second, given this evolution, it seems to make sense that the finite-amplitude eddy growth rate should scale as an eddy turnover scale, which is usually appropriate for the evolution of a developed eddy field. This eddy evolution scale is given by a length scale divided by a velocity scale where the obvious choice of eddy length scale is (19). There are two velocity scales that might be used: One is the scale for directly wind-forced velocity [(7)] along with (8). The alternative would be to assume that the eddy velocity goes as $\mathrm{EKE}_M^{1/2}$, and so (18) would yield the eddy velocity scale. It is found empirically that the former estimate is the better one, presumably because it is a better measure of the total speed of a typical particle, as opposed to the swirl velocity of an eddy. The resulting scaling is

$$\sigma_{\mathrm{NL}} \approx v^* \lambda_M^{-1} = a_3 f s^{-1} (1 + bs^2)^{1/2}, \quad (20)$$

where the coefficients b are those obtained in estimating EKE_M and differ for $\tau_A > 0$ or $\tau_A < 0$. Using this form, for $\tau_A > 0$, $a_3^+ = 0.0020$, the correlation is 0.43, and the rms error is 0.062 day^{-1}. For $\tau_A < 0$ (downwelling), $a_3^- = 0.0018$, the correlation is 0.57, and the rms error is 0.055 day^{-1}.

The growth rates are found to be slightly sensitive to bottom friction. Specifically, the expression (20) can be modified to account for dissipation so that

$$\sigma_{\mathrm{NL}} \approx a_3 f s^{-1} (1 + bs^2)^{1/2} (1 + \gamma\Omega)^{-1}, \quad (21)$$

where the frictional parameter Ω is defined by (10). For an upwelling context, $\gamma^+ = -0.4$, and the resulting error remains 0.062 day^{-1} (less than a 1% improvement), and for downwelling conditions, $\gamma^- = 1$ and the error decreases slightly to 0.052 day^{-1} (a 5% improvement). Thus, there is weak evidence that bottom friction decelerates growth under downwelling conditions.

d. Lateral mixing coefficient

A workable estimate for the lateral mixing coefficient is found to be the eddy swirl velocity magnitude squared (i.e., EKE_M) times a representative time scale f^{-1}. Other approaches to this scaling were attempted, but none performed as well as this one. Simply estimating

$$\kappa \approx a_4 a_1 E_0 (1 + bs^2)^{-1} f^{-1}, \quad (22)$$

and using the a_1 and b values from the EKE_M fit, yields a fairly useful result for the downwelling case but not the upwelling case. An additional empirical factor depending on s is found to improve this result considerably. Specifically,

$$\kappa \approx a_4 a_1 E_0 (1 + bs^2)^{-1} f^{-1} (1 + cs^2)^{-1}. \quad (23)$$

In this case, for $\tau_A > 0$, $c+ = 20$, and $a_4^+ = 0.70$, the correlation of the fit is 0.72, and the rms error is 4.6 m^2 s^{-1}. For $\tau_A < 0$, $c^- = 2$, and $a_4^- = 0.30$, the correlation is 0.84, and the rms error is 3.0 m^2 s^{-1}. Including this added ($c \neq 0$) correction decreases the rms error by 40% for the upwelling case and 17% for the downwelling case. Presumably, the added correction represents a tendency for a given cross-isobath flow to become less effective at lateral exchange (e.g., a weaker correlation of u and T) as the bottom becomes effectively steeper.

5. Discussion

All of the model runs presented here give rise to instability and a subsequent eddy field. The resulting spatially averaged eddy kinetic energy of the flow [(5c)] varies over about two orders of magnitude, however, depending especially on the strength of the wind impulse $|\tau_A|\Delta t$, the bottom slope α, the Coriolis parameter f, and the stratification N_I^2. Typical spatially averaged (spatial

maximum) eddy velocities are in the range of 0.001 to $0.02\,\mathrm{m\,s^{-1}}$ (0.01 to $0.07\,\mathrm{m\,s^{-1}}$), and dominant wavelengths are in the range of 3–55 km, although it is not clear that these values ought to be compared to observations where the present sort of isolated impulse forcing is not to be found. The main points of the present study are 1) to demonstrate that alongshore wind forcing, regardless of direction, is expected to give rise to baroclinic instability, hence an eddy field, and 2) to provide quantitative information on the dependence of key descriptors on initial parameters. The scaling analysis presented here, while not providing demonstrably unique results, does have the advantages of summarizing the model results in a compact form and of at least suggesting how wind-forced density perturbations ultimately drive instabilities and set the relevant space and time scales.

One particularly curious result is the finding that EKE does not depend substantially on the strength of bottom friction (as expressed by r), yet frictional dissipation (largely due to bottom stress) is of lowest-order importance in the evolution of EKE (Fig. 7). Other studies (Arbic and Flierl 2004; Brink and Cherian 2013) have shown that the dependence of an eddy field's properties on the frictional parameter can saturate for stronger damping, evidently due to a stratified spindown process. Nonetheless, understanding the generality and implications of this finding seems to call for further study.

It is, of course, always desirable to compare model results to observations, but it seems that the most relevant results are estimates of correlation length scales [such as those of Kundu and Allen (1976)], and these are not really comparable to the present model that does not have sustained fluctuating winds. The present, effectively initial-value problem ultimately gives rise to a fairly isotropic eddy field because continued fluctuating winds do not sustain large-scale alongshore current fluctuations. What can be said is that shelf baroclinic instability can give rise to currents with the length and amplitude scales suggested by the introduction to this contribution. Direct, resolved measurements of eddies on the conjectured scale on the shelf are rare, especially in topographically simple locations. However, there are a few hints of appropriately scaled eddies not obviously related to topographic irregularities; some hydrographic/SST measurements (Brink et al. 1984) and very high-frequency coastal radar measurements (Kim 2010; Bassin et al. 2005) are suggestive. A more useful comparison awaits a more realistic model and more complete observations.

Despite such caution, it is natural to ask whether the eddies found here, with horizontal eddy coefficients in the range of $1–20\,\mathrm{m^2\,s^{-1}}$ are likely to be substantial contributors to cross-shelf exchanges. A simple estimate can be had by comparing the importance of mixing to cross-shelf advection by means of a Pechlét number:

$$P = Lu^*\kappa^{-1}. \tag{24}$$

For a cross-shelf velocity scale u^*, it seems appropriate to consider the interior wind-driven cross-shelf velocity:

$$u^* \approx |\tau_A|(\rho_0 h_p f)^{-1}, \tag{25}$$

where h_p is a representative depth, and a reasonable cross-shelf scale might be the internal Rossby radius $N_I h_p f^{-1}$. Thus,

$$P \approx N_I|\tau_A|(\rho_0 f^2\kappa)^{-1}. \tag{26}$$

For the runs presented here (Table 1), the resulting Pechlét number ranges from around 1 to over 500, with 2–20 being typical. Thus, the preliminary result is that these resulting eddies do not dominate cross-shelf transports and are often negligible in this regard. This comparison, of course, is problematic because it compares an advective velocity representative of the early, wind-driven part of a model run to eddy mixing at much later stages.

Regardless of this specific comparison, it does appear that a very broad range of input parameters gives rise to substantial small-scale eddy motions over the shelf, regardless of the wind direction. These eddies certainly complicate the shelf flow pattern and thus make detailed descriptions of shelf flow more difficult to obtain as well as making deterministic shelf modeling more difficult. The added complexity associated with the eddy field should, in turn, be reflected in more complex and patchy biological and tracer distributions.

The present results, along with those of Durski and Allen (2005), have immediate potential relevance to ocean observations. It is common, in upwelling environments, to detect a general cooling of surface nearshore waters during strong, upwelling-favorable winds but then a flattening of isopycnals and generally shoreward motion of surface warmer waters after the wind weakens (e.g., Halpern 1976; Huyer 1984). This happens even in the absence of a substantial wind reversal. In the present, two-dimensional model, a burst of upwelling-favorable wind leads to a steady alongshore jet and no substantial subsequent tendency for isopycnals to flatten. On the other hand, when baroclinic instability is allowed in a three-dimensional model, the result is a flattening of isopycnals and weakening of the alongshore jet. It thus appears that instability mechanisms, which are difficult to detect because of the 5–10-km eddy scale,

may represent a general explanation for the ''relaxation'' phenomenon in the absence of complex coastal topography.

One of the newer aspects of this study is the focus on instabilities associated with downwelling. There is an extensive literature (much of it cited in the introduction) on the consequences of energetic upwelling-favorable winds; a front forms that intersects the surface, and the front becomes unstable. Further, there exist many measurements [e.g., those summarized by Barth (1989b)] that suggest that these instabilities occur in nature. The downwelling case is distinctly less studied, even though it is evident that downwelling can lead to the development (e.g., Allen and Newberger 1996; Austin and Lentz 2002) of a jet and a temperature structure that intersects the bottom rather than the surface. Observational evidence dealing specifically with downwelling configurations (e.g., Winant 1980; Austin and Barth 2002) is rather sparse, and there is little or no strong evidence for instability in the literature. Perhaps this is not surprising. Even if downwelling frontal instability were a dominant, energetic process, it would probably be difficult to detect with satellite sea surface temperature imagery, given that it implies weak or no initial surface temperature gradients. Other approaches for observing an instability (such as CTD sections, drifters, or towed, undulating bodies) would present their own issues in terms of synopticity or interpretability. Yet, for all this understandable lack of attention, the present results show that modeled instabilities due to downwelling winds are quite comparable, in terms of energy, scale, or growth rate, to instabilities associated with upwelling-favorable winds.

The present results, in summary, demonstrate that even modest ($0.01\ \mathrm{N\,m^{-2}}$) alongshore winds can generate cross-shelf density gradients that, through baroclinic instability, give rise to an eddy field that, in at least some cases, has the sort of velocity and length scales that are required in the proposed kinematic explanation for short u correlation scales. The scalings presented here are based on dynamical ideas that are consistent with this conjectured instability pathway. Yet, these results are only a first step in developing the case that wind-driven baroclinic instability can account for the correlation-scale conundrum. It needs to be shown that realistically time-dependent winds can lead to appropriately scaled eddies and how eddies due to shelf instabilities compare to those due to flow over rough topography. These remaining challenges will be the topic of future contributions.

Acknowledgments. This work was supported by the Woods Hole Oceanographic Institution and by the National Science Foundation, Physical Oceanography section through Grant OCE-1433953. Discussions with Hyodae Seo and Steve Lentz are greatly appreciated. Two anonymous reviewers provided very helpful comments.

REFERENCES

Allen, J. S., and P. A. Newberger, 1996: Downwelling on the Oregon continental shelf. Part I: Response to idealized forcing. *J. Phys. Oceanogr.*, **26**, 2011–2035, doi:10.1175/1520-0485(1996)026<2011:DCOTOC>2.0.CO;2.

Arbic, B. K., and G. R. Flierl, 2004: Baroclinically unstable geostrophic turbulence in the limits of strong and weak bottom Ekman friction: Application to midocean eddies. *J. Phys. Oceanogr.*, **34**, 2257–2273, doi:10.1175/1520-0485(2004)034<2257:BUGTIT>2.0.CO;2.

Austin, J. A., and J. A. Barth, 2002: Drifter behavior on the Oregon–Washington shelf during downwelling-favorable winds. *J. Phys. Oceanogr.*, **32**, 3132–3144, doi:10.1175/1520-0485(2002)032<3132:DBOTOW>2.0.CO;2.

——, and S. J. Lentz, 2002: The inner shelf response to wind-driven upwelling and downwelling. *J. Phys. Oceanogr.*, **32**, 2171–2193, doi:10.1175/1520-0485(2002)032<2171:TISRTW>2.0.CO;2.

Barth, J. A., 1989a: Stability of a coastal upwelling front: 1. Model development and stability theorem. *J. Geophys. Res.*, **94**, 10 844–10 856, doi:10.1029/JC094iC08p10844.

——, 1989b: Stability of a coastal upwelling front: 2. Model results and comparison with observations. *J. Geophys. Res.*, **94**, 10 857–10 883, doi:10.1029/JC094iC08p10857.

——, 1994: Short-wavelength instabilities on coastal jets and fronts. *J. Geophys. Res.*, **99**, 16 095–16 115, doi:10.1029/94JC01270.

Bassin, C. J., L. Washburn, M. Brzezinski, and E. McPhee-Shaw, 2005: Sub-mesoscale coastal eddies observed by high frequency radar: A new mechanism for delivering nutrients to kelp forests in the Southern California Bight. *Geophys. Res. Lett.*, **32**, L12604, doi:10.1029/2005GL023017.

Batchelor, G. K., 1953: *The Theory of Homogeneous Turbulence*. Cambridge University Press, 197 pp.

Blumsack, S. L., and P. J. Gierasch, 1972: Mars: The effects of topography on baroclinic instability. *J. Atmos. Sci.*, **29**, 1081–1089, doi:10.1175/1520-0469(1972)029<1081:MTEOTO>2.0.CO;2.

Brink, K. H., 1987: Coastal ocean physical processes. *Rev. Geophys.*, **25**, 204–216, doi:10.1029/RG025i002p00204.

——, 2011: Topographic rectification in a stratified ocean. *J. Mar. Res.*, **69**, 483–499, doi:10.1357/002224011799849354.

——, 2012: Buoyancy arrest and cross-isobath transport. *J. Phys. Oceanogr.*, **42**, 644–658, doi:10.1175/JPO-D-11-0143.1.

——, and S. J. Lentz, 2010: Buoyancy arrest and bottom Ekman transport. Part I: Steady flow. *J. Phys. Oceanogr.*, **40**, 621–635, doi:10.1175/2009JPO4266.1.

——, and D. A. Cherian, 2013: Instability of an idealized tidal mixing front: Symmetric instabilities and frictional effects. *J. Mar. Res.*, **71**, 425–450, doi:10.1357/002224013812587582.

——, and H. Seo, 2016: Continental shelf baroclinic instability. Part II: Oscillating wind forcing. *J. Phys. Oceanogr.*, **46**, 569–582, doi:10.1175/JPO-D-15-0048.1.

——, D. Halpern, and R. L. Smith, 1980: Circulation in the Peruvian upwelling system near 15°S. *J. Geophys. Res.*, **85**, 4036–4048, doi:10.1029/JC085iC07p04036.

——, D. W. Stuart, and J. C. Van Leer, 1984: Observations of the coastal upwelling region near 34°30′N off California: Spring 1981. *J. Phys. Oceanogr.*, **14**, 378–391, doi:10.1175/1520-0485(1984)014<0378:OOTCUR>2.0.CO;2.

——, J. H. LaCasce, and J. D. Irish, 1994: The effect of short-scale wind variations on shelf currents. *J. Geophys. Res.*, **99**, 3305–3315, doi:10.1029/93JC03034.

Chapman, D. C., 1987: Application of wind-forced, long, coastal-trapped wave theory along the California coast. *J. Geophys. Res.*, **92**, 1798–1816, doi:10.1029/JC092iC02p01798.

Charney, J. G., and M. Stern, 1962: On the stability of internal baroclinic jets in a rotating atmosphere. *J. Atmos. Sci.*, **19**, 159–172, doi:10.1175/1520-0469(1962)019<0159:OTSOIB>2.0.CO;2.

Dever, E. P., 1997: Subtidal velocity correlation scales on the northern California shelf. *J. Geophys. Res.*, **102**, 8555–8572, doi:10.1029/96JC03451.

Durski, S. M., and J. S. Allen, 2005: Finite-amplitude evolution of instabilities associated with the coastal upwelling front. *J. Phys. Oceanogr.*, **35**, 1606–1628, doi:10.1175/JPO2762.1.

——, ——, G. D. Egbert, and R. M. Samelson, 2007: Scale evolution of finite-amplitude instabilities on a coastal upwelling front. *J. Phys. Oceanogr.*, **37**, 837–854, doi:10.1175/JPO2994.1.

Feliks, Y., and M. Ghil, 1993: Downwelling-front instability and eddy formation in the eastern Mediterranean. *J. Phys. Oceanogr.*, **23**, 61–78, doi:10.1175/1520-0485(1993)023<0061:DFIAEF>2.0.CO;2.

Gill, A. E., and E. H. Schumann, 1974: The generation of long shelf waves by the wind. *J. Phys. Oceanogr.*, **4**, 83–90, doi:10.1175/1520-0485(1974)004<0083:TGOLSW>2.0.CO;2.

Haidvogel, D. B., H. G. Arango, K. Hedstrom, A. Beckmann, P. Malanotte-Rizzoli, and A. F. Shchepetkin, 2000: Model evaluation experiments in the North Atlantic basin: Simulations in nonlinear terrain-following coordinates. *Dyn. Atmos. Oceans*, **32**, 239–281, doi:10.1016/S0377-0265(00)00049-X.

Halpern, D., 1976: Structure of a coastal upwelling event observed off Oregon during July 1973. *Deep-Sea Res. Oceanogr. Abstr.*, **23**, 495–508, doi:10.1016/0011-7471(76)90861-5.

Holton, J. R., 1965a: The influence of viscous boundary layers on transient motions in a stratified rotating fluid: Part I. *J. Atmos. Sci.*, **22**, 402–411, doi:10.1175/1520-0469(1965)022<0402:TIOVBL>2.0.CO;2.

——, 1965b: The influence of viscous boundary layers on transient motions in a stratified rotating fluid: Part II. *J. Atmos. Sci.*, **22**, 535–540, doi:10.1175/1520-0469(1965)022<0535:TIOVBL>2.0.CO;2.

Huyer, A., 1984: Hydrographic observations along the CODE central line off northern California, 1981. *J. Phys. Oceanogr.*, **14**, 1647–1658, doi:10.1175/1520-0485(1984)014<1647:HOATCC>2.0.CO;2.

Jin, X., C. Dong, J. Kurian, J. C. McWilliams, D. B. Chelton, and Z. Li, 2009: SST–wind interaction in coastal upwelling: Oceanic simulation with empirical coupling. *J. Phys. Oceanogr.*, **39**, 2957–2970, doi:10.1175/2009JPO4205.1.

Karsten, R., H. Jones, and J. Marshall, 2002: The role of eddy transfer in setting the stratification and transport of a circumpolar current. *J. Phys. Oceanogr.*, **32**, 39–54, doi:10.1175/1520-0485(2002)032<0039:TROETI>2.0.CO;2.

Kim, S., R. M. Samelson, and C. Snyder, 2009: Ensemble-based estimates of the predictability of wind-driven coastal ocean flow over topography. *Mon. Wea. Rev.*, **137**, 2515–2537, doi:10.1175/2009MWR2631.1.

Kim, S. Y., 2010: Observations of submesoscale eddies using high-frequency radar-derived kinematic and dynamic quantities. *Cont. Shelf Res.*, **30**, 1639–1655, doi:10.1016/j.csr.2010.06.011.

Kundu, P. K., and J. S. Allen, 1976: Some three-dimensional characteristics of low-frequency current fluctuations near the Oregon coast. *J. Phys. Oceanogr.*, **6**, 181–199, doi:10.1175/1520-0485(1976)006<0181:STDCOL>2.0.CO;2.

Lozier, S., M. Reed, and G. Gawarkiewicz, 2002: Linear stability of shelfbreak fronts. *J. Phys. Oceanogr.*, **32**, 924–944, doi:10.1175/1520-0485(2002)032<0924:IOASF>2.0.CO;2.

Pedlosky, J., 1964a: The stability of currents in the atmosphere and the ocean: Part I. *J. Atmos. Sci.*, **21**, 201–219, doi:10.1175/1520-0469(1964)021<0201:TSOCIT>2.0.CO;2.

——, 1964b: The stability of currents in the atmosphere and the ocean: Part II. *J. Atmos. Sci.*, **21**, 342–353, doi:10.1175/1520-0469(1964)021<0342:TSOCIT>2.0.CO;2.

Pringle, J. M., 2001: Cross-shelf eddy heat transport in a wind-free coastal ocean undergoing winter time cooling. *J. Geophys. Res.*, **106**, 2589–2604, doi:10.1029/2000JC900148.

Spall, M. A., 2013: Dense water formation around islands. *J. Geophys. Res. Oceans*, **118**, 2507–2519, doi:10.1002/jgrc.20185.

Wijesekera, H. W., J. S. Allen, and P. Newberger, 2003: A modeling study of turbulent mixing over the continental shelf: Comparison of turbulent closure schemes. *J. Geophys. Res.*, **108**, 3103, doi:10.1029/2001JC001234.

Winant, C. D., 1980: Downwelling over the southern California shelf. *J. Phys. Oceanogr.*, **10**, 791–799, doi:10.1175/1520-0485(1980)010<0791:DOTSCS>2.0.CO;2.

——, 1983: Longshore coherence of currents on the southern California shelf during the summer. *J. Phys. Oceanogr.*, **13**, 54–64, doi:10.1175/1520-0485(1983)013<0054:LCOCOT>2.0.CO;2.

Winters, K. R., P. N. Lombard, J. J. Riley, and E. A. D'Asaro, 1995: Available potential energy and mixing in density-stratified fluids. *J. Fluid Mech.*, **289**, 115–128, doi:10.1017/S002211209500125X.